Full length article

Ultrahigh strength in lightweight steel via avalanche multiplication of intermetallic phases and dislocation

Sen Xiang [a,b], Xingtao Liu [a], Rong Xu [b], Fei Yin [c], Gary J. Cheng [a,d,*]

[a] School of Industrial Engineering, Purdue University, West Lafayette, IN 47906, United States
[b] School of Mechanical Engineering, Purdue University, West Lafayette, IN 47906, United States
[c] Hubei Key Laboratory of Advanced Technology for Automotive Components, Wuhan University, China
[d] School of Materials Engineering, Purdue University, West Lafayette, IN 47906, United States

A B S T R A C T

Lightweight high-strength steel has been an important topic for structural materials. Recent studies show that B2 intermetallic phase, nucleated around crystal defects such as grain boundaries and dislocations, can be used to further strengthen mechanical properties of metal alloys. Due to the limited density of nucleation sites, however, the current thermomechanical processing leads to formation of low density and coarse B2 phase. In this study, a lightweight steel Fe-Mn-Al-C (70 wt.% Fe) is processed by a thermal-controlled high strain rate plastic deformation process, warm laser shock peening (wLSP), in which high-density dislocations can be generated and high mobility of solute atoms at elevated temperature can facilitate the precipitation of B2 intermetallic phase. Simulations based on coupled phase-field and dislocation dynamics model are performed to investigate the intermetallic precipitation and dislocation formation during wLSP process. It is found that high density dislocations can be obtained in wLSP due to the pinning effect of B2 intermetallic phase on dislocations. The interaction between B2 intermetallic precipitates and shock wave facilitates the generation of high-density dislocations, which in turn serve as nucleation sites for B2 phase formation. This strong coupling effect results in avalanche multiplication of ultrahigh density and ultrafine B2 precipitates, and significant improvements in both strength and ductility. The yield strength of the lightweight steel reaches 2030Mpa with ultimate strength of 2850 MPa, among the highest for lightweight mid-carbon steel. This work provides a new insight to produce lightweight metals with ultrahigh density and ultrafine intermetallic phases for high strength and ductility.

© 2022 Published by Elsevier Ltd on behalf of Acta Materialia Inc.

1. Introduction

Developing lightweight high-strength steel has been a long-time challenge for structural materials, by manipulating the dislocations, grain structure, solid solution, nanoscale dispersion and second phases. Intermetallic phase, nucleated around crystal defects such as grain boundaries and dislocations, can be used to strengthen the mechanical properties of metal alloys. To improve the strength to weight ratio of steel, a lightweight alloy Fe-Mn-Al-C (density 6.5 g/cm³) has been developed by introducing low-density aluminum in steel. Depending on the content of Mn and C, the matrix phase can be ferrite, austenite, or a mixture of both (Duplex steel) [1,2]. For heavily alloyed steel, different types of precipitates can form with their size, morphology, and distribution tailored to enhance their mechanical properties. Lin et al. [3]. reports that high-density nano-sized κ-carbides ((Fe, Mn)$_3$AlC type) can precipitate from as-quenched austenite matrix after aging at 550 °C for 15 h, and the material reaches high yield strength up to 1100 MPa. However, κ-carbides can be easily sheared by dislocations, and this limits their capability to strengthen metals [4]. Plastic deformation can be used to induce the nucleation and formation of fine precipitates with high densities [5]. The main idea is to introduce defects in the matrix to facilitate the precipitation process. Kim et al. [6]. has successfully introduced B2 phase which nucleates on grain boundaries and deformation shear bands after hot rolling. Hard FeAl-B2 type intermetallic precipitates are dispersed in the austenite matrix to improve the strength. Further study shows that austenite matrix with B2 phase embedded has high hardness around 8.2 GPa [7]. While strength of steel can be improved after introducing hard B2 with traditional heat treatment or hot rolling, currently the B2 precipitates are coarse (200–1000 nm) and some brittle stringer bands are present, such that strength and ductility cannot be achieved simultaneously. Precipitation of ultrafine intermetallic B2 phase with uniform distribution

* Corresponding author.
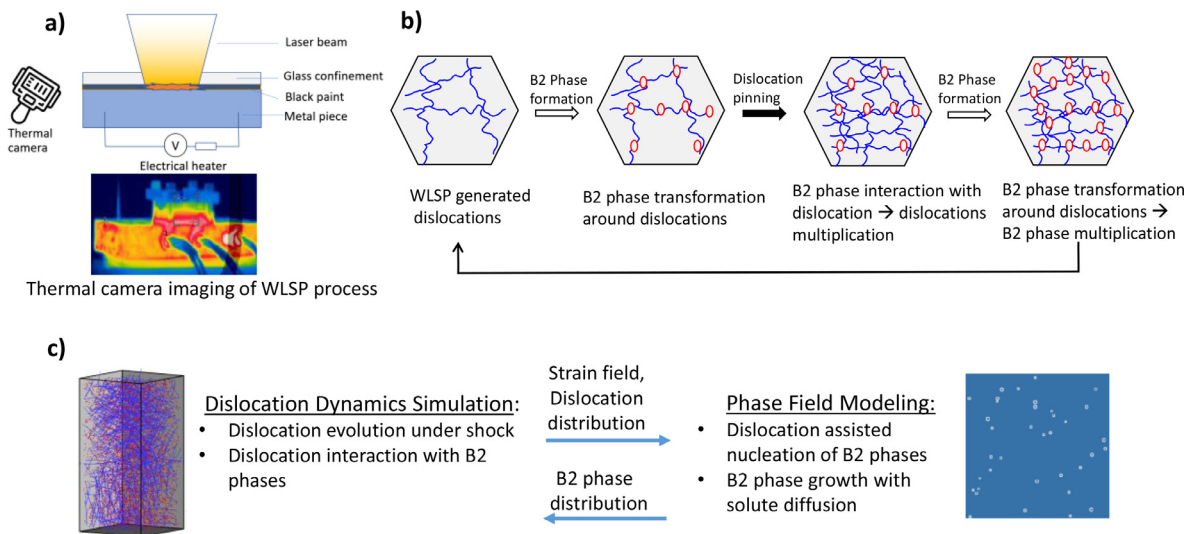 E-mail address: gjcheng@purdue.edu (G.J. Cheng).

Fig. 1. a) schematic view of warm laser peening process. b) the avalanche formation of dislocation and precipitates during warm laser shock peening process. c) coupled phase-field and dislocation dynamics model to simulate evolution of precipitates and dislocations.

is critical to further improve the mechanical properties of metal alloys.

Laser shock peening (LSP) is a high strain rate plastic deformation process. During laser shock peening, large shock pressure generated by the plasma transmits to the substrate and plastically deforms the material [8]. Processing temperature plays an important role on the strength and microstructures [9]. By preheating the substrate to an elevated temperature, precipitates may form [10]. Ye and Liao [11,12] find out that high-density $MgZn_2$ particles or 10 nm carbides can precipitate from matrix when preheating the aluminum alloy 7075 to 250 °C or AISI 4140 steel to 300 °C. Warm laser shock peening (wLSP) process is a thermal-mechanical process combining dislocation generation and dynamic precipitation formation. As shown in Fig. 1a), high strain rate plastic deformation results in some dislocations. These newly generated dislocations provide favored nucleation sites for precipitates. With warm temperature facilitating the diffusion of solute atoms, nucleation rate is greatly increased, and dynamic precipitation occurs. The presence of precipitates pin dislocations and hinder dislocation movements during plastic deformation. For deformation to continue, more new dislocations need to be generated which supply more nucleation sites. In this way, high-density dislocations and uniformly distributed nano precipitates can be generated in a short time. wLSP can be more effective to generate high density nanoscale precipitates because dislocation density generated by wLSP can be much higher compared to shear bands generated by hot rolling.

Computational modeling has been used extensively to understand the phase change and plastic deformation during thermomechanical processing. Phase-field method has been widely used for solidification and precipitation simulations, such as γ' precipitates in Ni-based superalloy [13], Ni_3Al precipitation in Ni-Al alloy [14], $Mg_{17}Al_{12}$ precipitation in Mg-Al alloy [15], and Al_2Cu precipitation phase in Al-Cu alloy [16]. Dislocation dynamics model can simulate the evolution of dislocations under plastic deformation by solving governing equations of dislocation motion [17,18]. Dislocation behavior under laser shock peening has been simulated by dislocation dynamics model [19,20]. It can also take into account the pinning effect by precipitates [21]. Wu et al. has tried to couple a 2D phase-field model with a dislocation dynamics model to study dislocation piling ups at precipitates in nickel-based superalloy [22].

In this study, warm laser shock peening is applied to low-density Fe-Mn-Al-C steel. Different preheating temperatures are tested to evaluate their effect on microstructures and mechanical properties. Microstructure evolution during wLSP includes dislocation formation and intermetallic phase precipitation. To illustrate the coupling effects of avalanche multiplication of both dislocations and precipitates during wLSP, simulations based on coupled phase-field and dislocation dynamics model are performed and validated by experiments.

2. Material and experimental methods

Sample preparation: Compositions of high-manganese low-density steel used in this study are the following (wt.%): C 1.0%, Mn 17.5%, Al 10.4%, Ni 3.4%, and balance Fe. Nickel is added to catalyze B2 precipitation. The material is produced by an induction melting furnace. Before LSP, samples are solution treated at 1050 °C for 2 h with argon as a protective gas and then water quenched.

Warm laser shock peening process: For this experiment, Nd-YAG laser (Surelite III, Continuum, Inc.) with 5 ns pulse width, 1 mm beam diameter is used. Aluminum foil is attached to the sample as a sacrifice layer and BK7 glass is adopted as confining media. Samples are laser shock peened at room temperature and higher temperatures 200 °C, 300 °C, 350 °C, 400 °C, 450 °C. This is achieved by preheating a copper block with three 300 W cartridge heaters from Omega Engineering. A FLIR A320 infrared camera is used to monitor the preheating temperature. All samples are then annealed at 900 °C for 20 mins.

Microstructure characterization: Bruker D8 Focus X-ray diffractometer with Cu K-alpha source is used for phase analysis. Transmission electron microscopy (TEM) samples are prepared by a lift-out method using the focused ion beam (FIB) technique with the Thermo Scientific Helios G4 SEM/FIB Dual-beam system. To characterize microstructures after processing, TEM images are obtained using an FEI Talos 200X TEM operated at 200 kV.

Mechanical property characterization: Surface hardness for solution treated and laser processed samples are measured by nanoindentation tests using Agilent Technologies Nano indenter G200 with a standard Berkovich diamond indenter under a load of 200mN.

To test the mechanical properties, micropillars are fabricated by FIB technique using FEI Nova 200 SEM/FIB Dual-beam system. They

have a cylindrical geometry with a diameter of 3 μm and length around 8 μm. Micropillar compression tests are performed at room temperature using the same nanoindenter equipped with a diamond flat tip. All measurements are conducted at a constant strain rate of 0.05 s^{-1} and the same displacement of 2000 nm with 1 s hold.

3. Coupled phase-field and dislocation dynamics model

To illustrate the evolution of precipitates and dislocations and interactions between them during laser shock peening, coupled phase-field and dislocation dynamics model has been proposed. (Fig. 1b)). In the coupled model, the phase-field model simulates the B2 nucleation at high-density dislocation sites and precipitation growth during wLSP. Dislocation dynamics model simulates the dislocation formation and multiplication under shock pressure, and dislocation pinning by precipitates.

3.1. Phase-field model

The Phase-field method is adopted to simulate the isothermal precipitation of the B2 intermetallic phase for Fe-Al binary alloy during the laser shock peening process. Phase-field model used for this study is proposed by Kim et al. [23]. The governing equation for the time evolution of order parameter is:

$$\frac{\partial \eta}{\partial t} = -M \frac{\delta F}{\delta \eta} \tag{1}$$

Where η is the order parameter varying from 0 to 1 to distinguish the matrix and precipitate (η=0, matrix; η=1, precipitate). M is the interface mobility coefficient. F is the total free energy of the system, including chemical free energy and gradient energy, given by:

$$F(c, \eta) = \int_V \left[f(c, \eta) + \frac{1}{2}\varepsilon^2 (\nabla \eta)^2 \right] dV \tag{2}$$

Here f is the chemical free energy density of the system written as

$$f(c, \eta) = (1 - h(\eta))f^\gamma(c_\gamma) + h(\eta)f^{\gamma'}(c_{\gamma'}) + wg(\eta) \tag{3}$$

Where $f^\gamma(c_\gamma)$ and $f^{\gamma'}(c_{\gamma'})$ are the chemical free energy densities of the matrix and precipitate [24]. h(η) is an interpolation function varying from 0 to 1. g(η) is the double-well potential and w is the height of the double-well potential. In this work, the following h(η) and g(η) are used:

$$h(\eta) = \eta^3(6\eta^2 - 15\eta + 10) \tag{4}$$

$$g(\eta) = \eta^2(1 - \eta)^2 \tag{5}$$

The governing equations for time evolution of concentration is:

$$\frac{\partial c}{\partial t} = \nabla \cdot \left(\frac{D(T)}{f_{cc}} \nabla(f_c) \right) \tag{6}$$

Where D(T) is the solute diffusivity, which is dependent on temperature T. f_c and f_{cc} are the first and second order derivatives of the energy density f with respect to concentration c.

In the KKS model, the interface region is assumed to be a mixture of the matrix and precipitate phase with different compositions, but equal chemical potential:

$$c = (1 - h(\eta))c_\gamma + h(\eta)c_{\gamma'} \tag{7}$$

$$\frac{df^\gamma(c_\gamma)}{dc_\gamma} = \frac{df^{\gamma'}(c_{\gamma'})}{dc_{\gamma'}} \tag{8}$$

Table 1
Phase-field simulation parameters.

Mesh size	1nm
time step	0.01ns
M interface mobility coefficient	0.374
w height of double well potential	673,200,000
D solute diffusivity	$0.18119 \times \exp(-253,560/(8.134 \times T))$

Where c_γ and $c_{\gamma'}$ are the concentration of solute atom in the matrix and precipitate phase at the interface region. They can be solved by the above two equations. Table 1 lists parameters used in the phase-field model [24].

Precipitation in Fe-Al alloy involves the formation of B2 intermetallic particles from the solid solution. Higher density dislocations generated during laser shock peening can provide nucleation sites and thus have a big impact on the precipitation process. To incorporate this effect into the model, modified classical nucleation theory proposed by Yuhki et al. [25]. is adopted.

Due to the high computational cost of 3D phase-field model, a 2D phase-field model is used in this study. The model has 400 × 400 cells with 1 nm uniform mesh size. Both the phase-field and concentration equations are solved by an explicit finite difference scheme. Zero flux boundary conditions are used for the phase-field and concentration governing equations. Randomly distributed dislocations with the density of $1 \times 10^{10} \text{m}^{-2}$ are used to initialize the simulation. After that, dislocation distribution results from the dislocation dynamics model are used.

3.2. Dislocation dynamics model

The dislocation dynamics (DD) model is used to investigate dislocation multiplications and their interactions with precipitates during laser shock peening. The simulations are performed to mimic shock loading with a high strain rate ($>10^6$/s) and short pulse duration (few nanoseconds). In the DD model, dislocations are discretized into segments and the velocity v of a dislocation segment 's' is governed by the equation of motion as follows [20]:

$$m_s \dot{v} + \frac{1}{M_s(T, P)} v = F_s \tag{9a}$$

$$\begin{aligned} F_s = {} & F_{Peierls} + F_D + F_{Self} + F_{External} + F_{Obstacle} + F_{Image} \\ & + F_{Osmotic} + F_{Thermal} \end{aligned} \tag{9b}$$

In the above equation, m_s is the effective dislocation segment mass density. Ms is the dislocation mobility which depends on temperature T and pressure P. The driving force F_s consists of Peierls stress $F_{Peierls}$, dislocation-dislocation interaction force F_D, dislocation self-force F_{Self}, externally applied force $F_{External}$, dislocation obstacle interaction force $F_{Obstacle}$, image force F_{Image}, osmotic force $F_{Osmotic}$ and thermal force $F_{Thermal}$.

In the present analysis, the dislocation dynamics simulation is performed using multiscale dislocation dynamics plasticity (MDDP) code [17]. The simulated matrix is single crystal austenite, with a face-centered cubic structure and a block size of 4000 b × 4000 b × 8000 b, where $b = 0.265$ nm is the magnitude of the Burgers vector. To begin with, an initial dislocation density of $1 \times 10^{10} \text{m}^{-2}$ is adopted by randomly placed in the block five Frank-Read dislocation sources of 20b~100b in length. Frank-sessile loops are used to represent the precipitates. During the simulation, dislocations interact elastically with sessile loops, which models the pining effect. Some of the parameters used for dislocation dynamics are listed in Table 2. For dislocation mobility, it is strongly

Table 2
Dislocation dynamics simulation parameters.

Parameter	Density(Kg/m^3)	ShearModulus (Pa)	Poisson ratio	Mobility((Pa·s)$^{-1}$)	Stacking fault energy (J/m^2)
Value	7870	8×10^{10}	0.27	$1/(2.6 \times 10^{-8} \times T + 2.5 \times 10^{-5})$	0.080

temperature-dependent and the formula is taken from Chu et al. [26].

The phase-field model and dislocation dynamics model alternately runs with data exchanging between them. To begin with, the phase-field model runs with a given initial dislocation density. After evolution, the size and distribution of the precipitates can be obtained. The precipitates are then incorporated into the dislocation dynamics model using Frank-sessile dislocation loops. Then dislocation generation under shock pressure and dislocation precipitate interactions are investigated. After that, dislocations obtained from the DD model will be taken into the phase-field model to simulate the dislocation-assisted precipitation. The data conversion between 2D phase-field and 3D dislocation dynamics is based on the stereological relations [27]. To convert the B2 phase distribution from 2D phase-field to 3D dislocation dynamics model, the following steps are followed: 1) get the number, size distribution, and mean diameter D from phase-field model. 2) convert the number density from 2D to 3D by $N_V = N_A/D$. 3) incorporate Frank-sessile loops in dislocation dynamics model with the calculated number to mimic the precipitates. Since the data conversion between phase-field and dislocation dynamics is complex and done manually, only two iterations are used for the moment.

4. Results

4.1. Mechanical properties

Nanoindentation tests are performed to measure the hardness after laser shock peening. As Fig. 2a) shows, the hardness after solution treated is 6.4 GPa. For laser shocking peening at room temperature, the hardness is improved to 7.6 GPa. And hardness can reach 8.9 GPa when the preheating temperature is gradually increased to 400 °C. However, the material will become softer, and the hardness is only 8.4 GPa if the preheating temperature is 450 °C.

To further investigate the mechanical properties, micropillars are made from the solution treated, LSP, wLSP (200 °C and 400 °C) samples, and pillar compression tests are performed. The true stress-strain curves are shown in Fig. 2b) and Scanning Electron Microscopy (SEM) images of pillars after compression are presented in Fig. 2c)-f). After the solution treatment, the yield strength is around 850 MPa. Multiple parallel slip lines can be observed on the pillar indicating cross slip happens during compression (Fig. 2c)). Yield strength for room temperature LSP sample can reach 1450 MPa (an increase of 70%). The deformation mode has changed from cross slip to single slip, which can be observed in Fig. 2d). wLSP at 200 °C can increase the yield point to 1600 MPa. The pillar deforms in a similar pattern with slip lines in one direction. Increasing preheating temperature to 400 °C, the yield strength can reach 2030 MPa, which has a significant improvement of 130%. There might be some size effect compared to macro compression test. But the pillars tested in this work have the same size, thus the comparison among themselves can provide valuable information.

XRD analysis has been used to identify the phase change during the process, and results are presented in Fig. 3. As we can see, only austenite is observed for solution treated sample, with the peak at (111)γ, (220) γ, (311) γ, and (222) γ.

The initial microstructure is pure austenite and free from the B2 phase. However, 25 °C LSP sample and the 400 °C wLSP sample have several extra peaks demonstrating the presence of FeAl-B2 intermetallic phase at (110) and (211). And higher peaks for warm processed samples indicate a higher percentage of B2 precipitates.

4.2. Microstructure characterizations

Transmission Electron Microscopy (TEM) images from the samples prepared by the FIB technique are used to identify the microstructures under different processing temperatures. After room temperature LSP, both dislocations (marked by blue arrows) and nanoparticles (marked by red arrows) can be observed in Fig. 4a). As we can see, some B2 nano precipitates (several nanometers) are distributed randomly and uniformly around the dislocation networks. LSP at 400 °C shows a much higher density of dislocation tangles and precipitates (Fig. 4c). The dislocation lines and precipitates after LSP at 200 °C is shown in Fig 4b), which is non-uniform and has density between that from 25 °C and 400 °C. Selected Area Electron Diffraction (SAED) pattern for the matrix is presented in Fig. 4f), and the zone axis is in [1 1 2]. The High-Resolution Transmission Electron Microscopy (HRTEM) image in Fig. 4g) has shown one nanoparticle with a size of 15 nm and the lattice parameter is measured to be 0.287 nm. This is close to 0.285 nm of FeAl-B2 lattice parameter predicated by first-principle calculations [28]. Its corresponding Fourie Transformation (FFT) pattern is presented in Fig. 4h), which shows the zone axis of [111] of the BCC structure.

Fig. 4d) and e) present a dark-field TEM image for the sample laser shock peeing processed at 25 °C. A quantitative analysis is performed to characterize its particle distribution and dislocation density. The size of the image is 400 nm × 400 nm, and the total number of particles are 28 with a size around 10 nm. Dislocation density is determined by the Smith-Guttman linear intercept method by the following equation [29,30]:

$$\rho_D = \frac{2N}{Lt} \tag{10}$$

Where N is the number of intercepts between lines and dislocations (17), L is the total length of randomly placed lines (yellow lines 1300 nm), and t is the thickness of the foil (100 nm). Dislocation density for laser shock peening at 25 °C is calculated to be 2.6×10^{14} m^{-2}.

5. Discussion

Experiment results show that the laser shock peening process can introduce high density dislocations and B2 intermetallic precipitates in Fe-Al-Mn-C steel. Dislocation density is about 2.6×10^{14} m^{-2} for room temperature LSP. Precipitates are ultrafine in nano size and no stringer bands are present. By increasing the preheating temperature, more B2 precipitates can form which is confirmed by both XRD analysis and TEM images. And maximum yield strength of 2030 MPa can be obtained at an optimal 400 °C preheating temperature. To understand the formation mechanisms of dislocations and precipitates as well as the role preheating temperature plays in their formation, a coupled phase-field and dislocation dynamics model is employed to calculate the particle and dislocation evolution during LSP at five different temperatures: 25 °C, 200 °C, 300 °C, 400 °C, 450 °C.
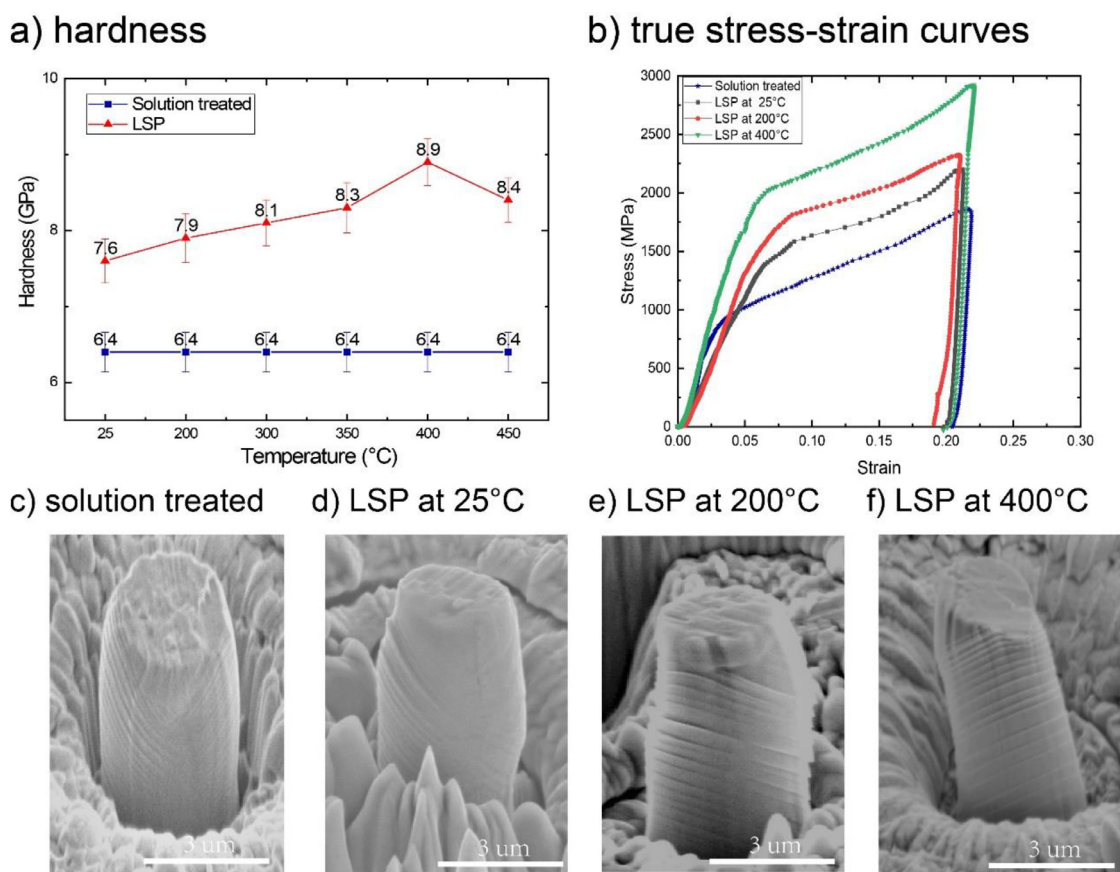
Fig. 2. Mechanical properties. a) hardness of solution treated sample and LSP processed samples. b) trues tress strain curves after micropillar compressions for solution treated and LSP processed samples. (c)-(f) corresponding SEM images of micropillars after compression.
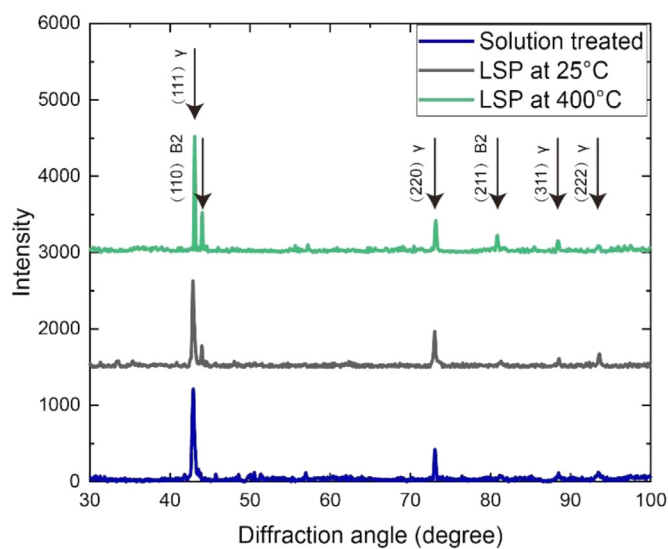

Fig. 3. XRD patterns of solution treated and laser shock peening processed samples.
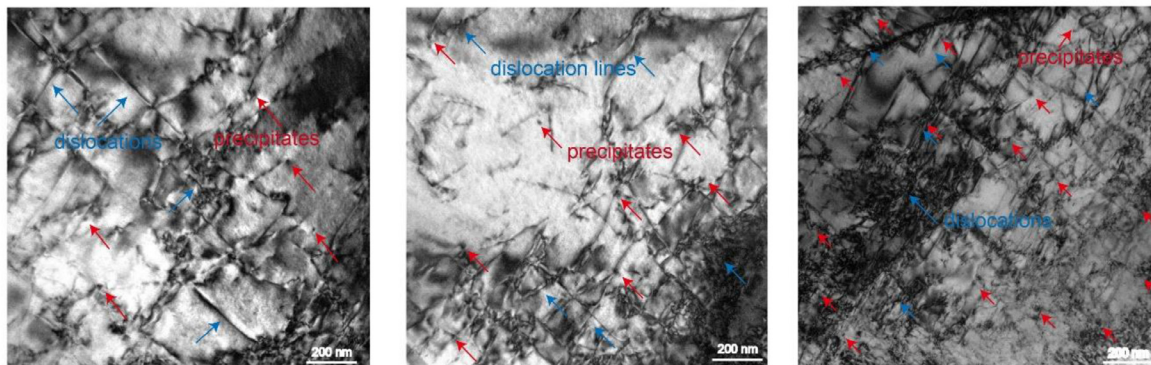
5.1. Precipitate evolution

The evolution of precipitates at 25 °C and 400 °C are presented in Fig. 5. The number of particles for LSP 25 °C gradually increases as time evolves: 7, 12, 22 and 29. And precipitates grow into a spherical shape and become larger as solute atoms moving towards the nucleus. As we can see, particles are randomly distributed. A

good agreement between predicated and measured precipitation distribution is achieved. Similar trend is observed for LSP 400 °C, except that more particles 7, 13, 32 and 43 are present and particles are larger in general. This can be ascribed to the higher growth rate as solute atoms can diffuse much faster at higher temperature.
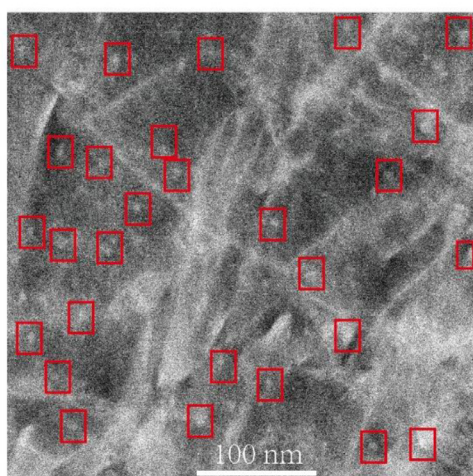
Fig. 6 presents the dislocation induced von mises stress field σ_1 at $t = 10$ ns obtained from the DD model at different temperatures. Multiple spikes with high stresses up to 2–8 GPa can be observed. These localized high stress spots are due to the presence of dislocations generated by shock load. And they can provide nucleation sites for the precipitation formation. Fig. 7a) shows the area percentage of precipitates under different temperatures. Here, area percentage is the total area of all precipitates divided by the total area of the simulation cell. The area percentage is increasing monotonically, and it grows faster after 10 ns when initial low dislocation density is updated by high dislocation density from the DD model. The growth rate slows down finally as solute atoms in the matrix are gradually depleted. The final percentages are 2.3%, 3.4%, 3.9%, 5.0% and 5.6% for 25 °C, 200 °C, 300 °C, 400 °C, 450 °C respectfully. The area percentage almost doubles at elevated temperature.

To have a more detailed investigation, precipitates are categorized into different size groups: 0–5 nm, 5–10 nm, 10–15 nm, 15–20 nm, 20–25 nm. Its size distributions are summarized in Fig. 7b)-f), which vary greatly with temperature. After first iteration of phase-field simulation ($t = 10$ ns), particle numbers are close: 12, 13, 13, 13, 13. But the particle sizes are different: higher temperature process tends to have more particles between 10 and 15 nm and fewer particles between 0 and 5 nm. This also reflects in the area percentage: higher temperature has higher percentage 0.8%,
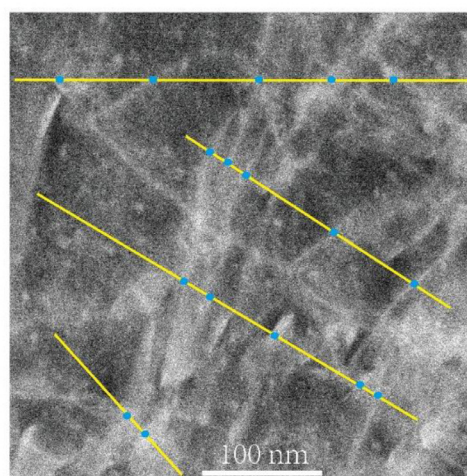
Fig. 4. Bright field TEM images showing dislocations and B2 intermetallic precipitates for a) laser shock peening at 25 °C. b) laser shock peening at 200 ° c) laser shock peening at 400 ° d) particle distributio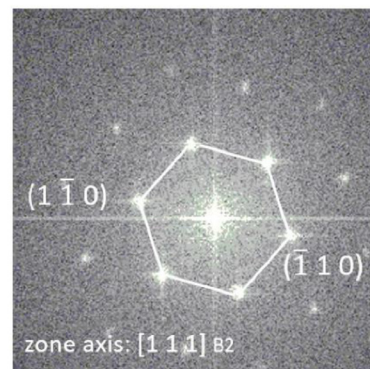n marked by red box for LSP at 25 °C. e) dislocation density measured by random yellow lines for LSP at 25 °C. f) selected area electron diffraction pattern for matrix. g) high resolution TEM image showing one precipitate. h) Fourier transform pattern for HR TEM image.
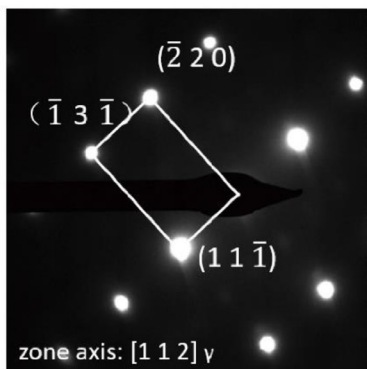
1.0%, 1.1%, 1.3% and 1.4%. After the second iteration of phase-field simulation ($t = 20$ ns), particle numbers increase to 29, 34, 38, 43, 42. Large differences can be seen in particle numbers and sizes.

Phase-field simulations have shown the precipitation evolution during laser shock peening. Nucleation of B2 intermetallic phase is aided by dislocations serving as nucleus site, and precipitates grow as solute atoms diffusing towards them. Processing temperature plays an important role on its final distribution due to its effect on solute atom diffusivity. At room temperature, particles have a small quantity and small precipitates(0–15 nm) dominate the sam-

ple. For elevated temperature, more particles are present and large precipitates are dominant.

5.2. Dislocation evolution

Dislocation behavior at high strain rate deformation is investigated under elevated temperature with the presence of precipitates. Fig. 8 shows the dislocation evolutions for LSP 25 °C and 400 °C from the dislocation dynamics simulation. Blue lines represent dislocations and red lines represent particles. Initially($t = 0$ ns), five Frank-Read sources are placed. As time evolves,
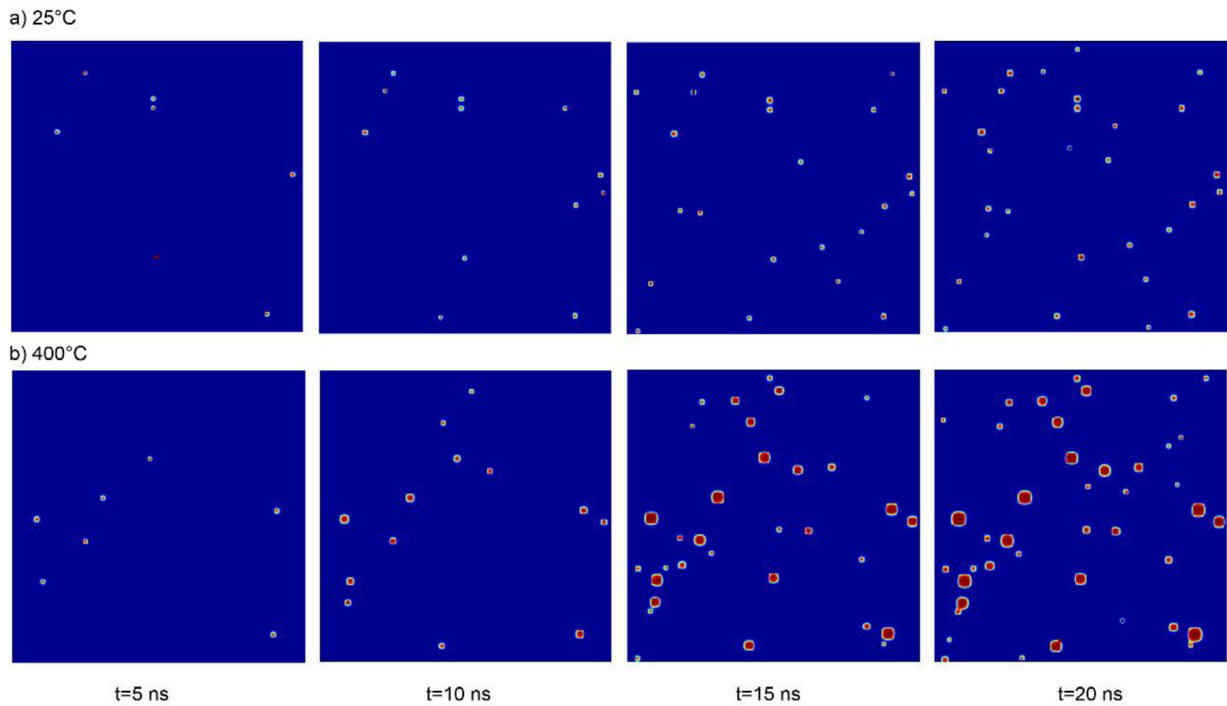
a) 25°C

b) 400°C

t=5 ns   t=10 ns   t=15 ns   t=20 ns

Fig. 5. Results of phase-field simulation for particle evolution after laser shock peening at *t* = 5 ns, 10 ns, 15 ns and 20 ns. a) 25 °C and b) 400 °C.
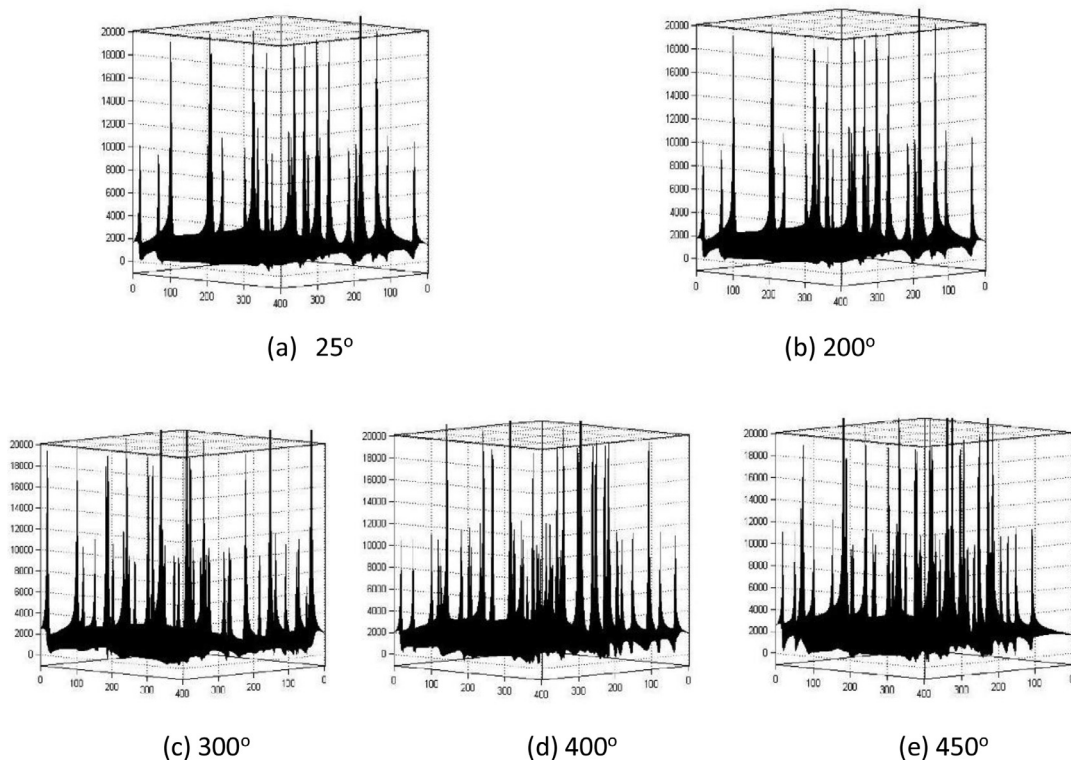

(a) 25°

(b) 200°

(c) 300°

(d) 400°

(e) 450°

Fig. 6. Von Mises stress σ_1 induced by dislocation microstructure at 25 °C, 200 °C, 300 °C 400 °C and 450 °C.

dislocations emit from these sources, and they interact with the particles. Dislocations fill the simulation box and they distribute uniformly eventually. Simulation results show there are more dislocation lines at 400 °C than 25 °C, which matches well with the experiment results showed in Fig. 4a) and c).

Dislocation density under different temperatures is plotted in Fig. 9a). The dislocation density evolution can be divided into three stages: 1) the stable stage. Dislocation density is constant during elastic deformation. 2) the rapid increasing stage. Dislocations multiply quickly as plastic deformation initiates. 3) the slow growing stage. Dislocation growth rate decreases due to the high existing dislocations. Final dislocation density is $3.26 \times 10^{14}\ m^{-2}$, $4.78 \times 10^{14}\ m^{-2}$, $5.62 \times 10^{14}\ m^{-2}$, $6.14 \times 10^{14}\ m^{-2}$, $6.40 \times 10^{14}\ m^{-2}$ respectfully. A reasonable agreement between
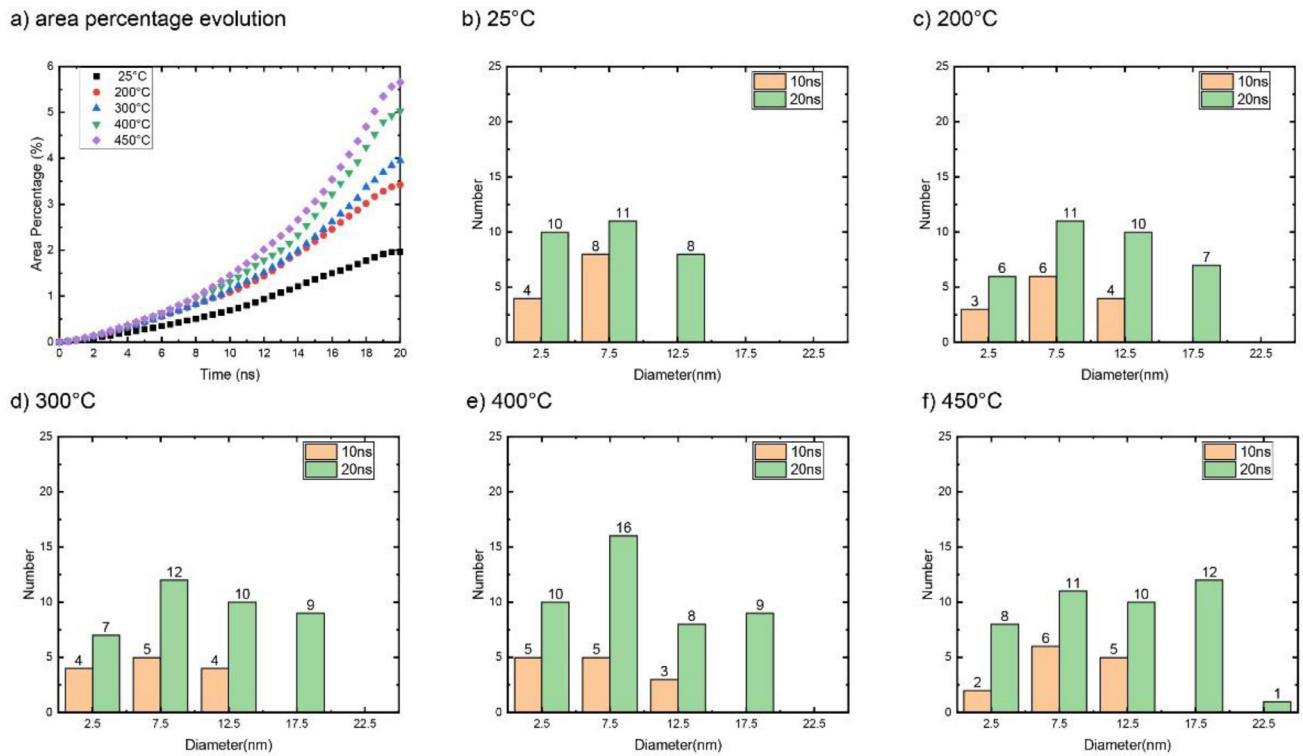
Fig. 7. Results of phase-field simulation for particle evolution. a) area percentage evolution at 25 °C, 200 °C, 300 °C 400 °C and 450 °C. b)-f) particle size distribution at $t = 10$ ns and 20 ns for 25 °C, 200 °C, 300 °C 400 °C and 450 °C respectfully.
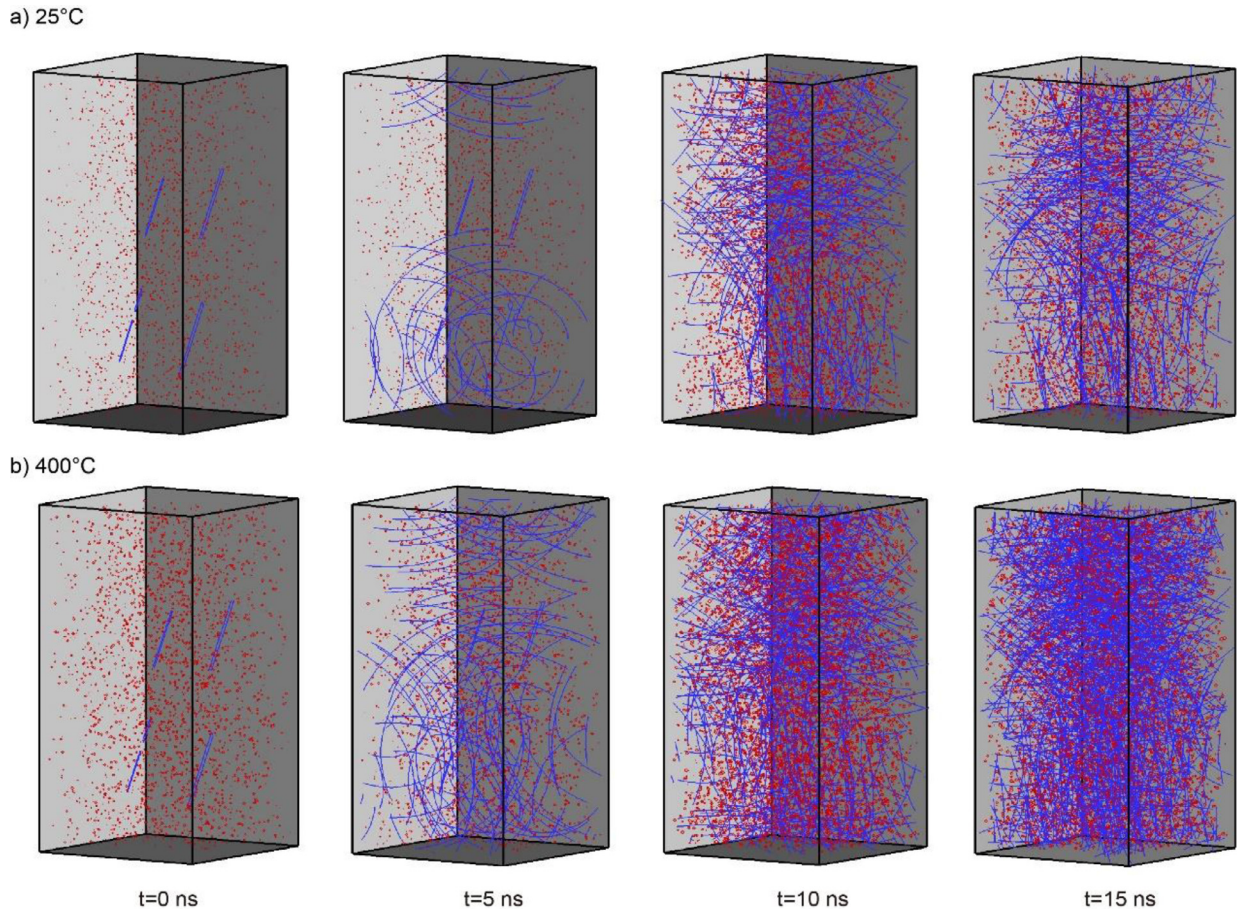

Fig. 8. Dislocation dynamics results for dislocation generation and movements at $t = 0$ ns, 5 ns, 10 ns and 15 ns. (blue lines represent dislocations and red lines represent particles) a) laser shock peening at room temperature; b) warm laser shock peening at 400 °C.
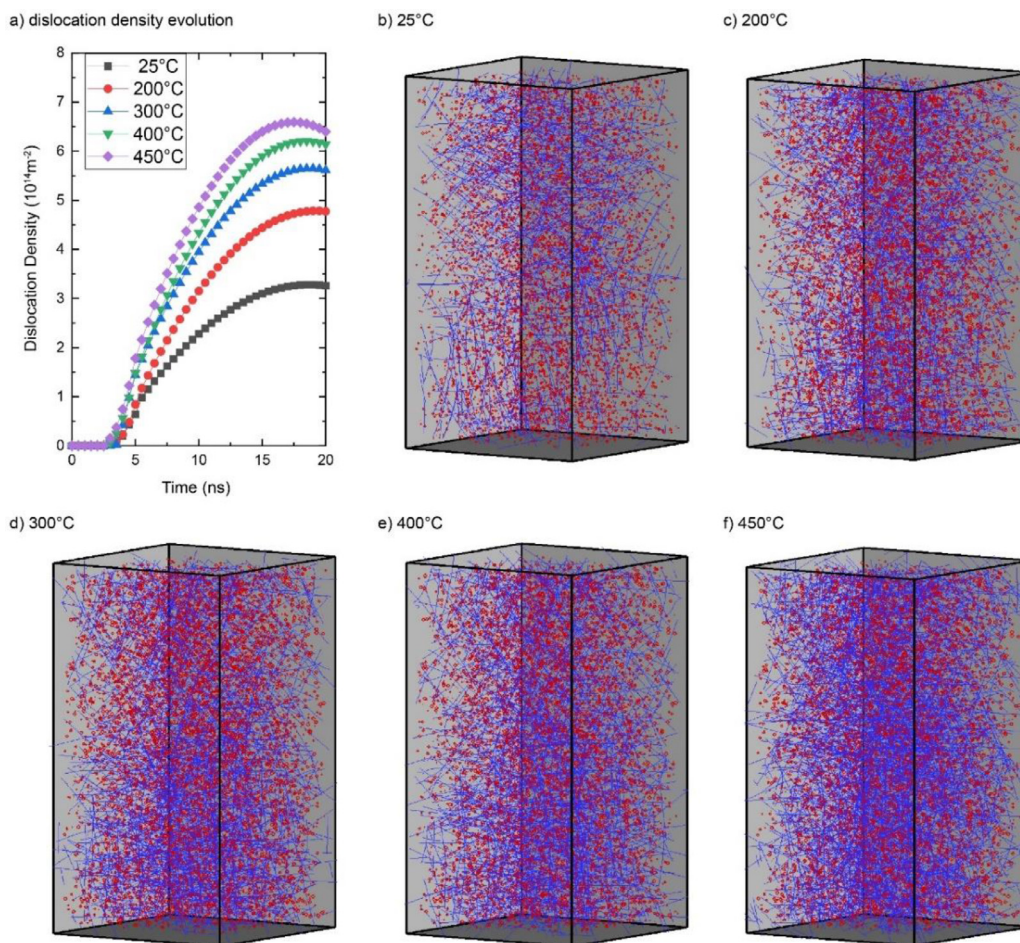
Fig. 9. Results of DD simulation for dislocation evolution. a) dislocation density evolution at 25 °C, 200 °C, 300 °C 400 °C and 450 °C. b)-f) dislocation and particle distribution at $t = 20$ ns for 25 °C, 200 °C, 300 °C 400 °C and 450 °C respectfully.

predicted and measured dislocation density for LSP at 25 °C is achieved. To be noticed, a small drop in the dislocation density can be observed at the later stage for LSP at 450 °C. The decrease is because dislocation annihilation begins to dominate over dislocation multiplication as temperature rises. At $t = 20$ ns, the dislocation density for 450 °C is still larger than 400 °C. But it will become less with longer simulation time due to its quicker drop speed. The hardness decreases at 450 °C compared to 400 °C is ascribed to the lower dislocation density because of dislocation annihilation. The final dislocation distributions are presented in Fig. 9b)-f), and they are randomly and uniformly distributed in the simulation box with particles embedded among them.

The dislocation density evolution is also highly sensitive to working temperature. More dislocation lines and tangles are observed at higher temperature. Similar phenomenon has also been reported by Song et al. [31], where higher dislocation density is observed after deformation at 200 °C than at 25 °C. This can be attributed to: (1) weak dislocation annihilation since the processing time is ultrashort (several nanoseconds); (2) more dislocation generation to accommodate plastic deformation as precipitates generated at higher temperatures have a better pining effect on dislocations.

5.3. Avalanche multiplication of precipitates and dislocations

Based on the particles and dislocations observed in TEM images and their evolutions demonstrated by coupled phase-field and dislocation dynamics model, the avalanching multiplication of precipitates and dislocations are proposed during warm laser shock pee-

ing. I) Dislocations assist precipitates formation. High density dislocations generated by plastic deformation serve as nucleation sites, leading to formation of high density B2 precipitates. Nano precipitates can distribute evenly around dislocation networks within the material. II) Precipitates boost dislocation generation. High density precipitates pin dislocation movements and more dislocation generation is required to allow deformation to continue. These two effects happen simultaneously and foster each other. The result of the avalanching process is high density of both dislocations and B2 precipitates. By increasing the deformation temperature, precipitates can grow faster with higher atom diffusivity and dislocations move slower with a larger drag effect. Higher density dislocations and B2 precipitates can be achieved.

6. Conclusions

In this work, warm laser shock peening process is applied on Fe-Al-Mn-C lightweight steel. Experiment results show that the laser shock peening process can successfully introduce high density dislocations and nano intermetallic B2 precipitation in the steel, without large stringer bands. By increasing the preheating temperature to 400 °C, both densities of B2 nanoprecipitates and dislocations can be increased dramatically, and the yield strength reaches 2030Mpa. The great improvement of mechanical property is ascribed to the combination of strain hardening and nanoprecipitation hardening. Coupled phase-field and dislocation dynamic model are used to simulate microstructure evolution during warm laser shock peening. The phase-field model simulates the precipitation nucleation and growth, and the dislocation dynamics model

simulates the dislocation generation and movement. A good agreement between experimental and predicated particle distribution and dislocation density is achieved, and avalanching multiplication of precipitates and dislocations is illustrated. Coupled phase-field and dislocation dynamics model is promising for the prediction of complex phase transformation and dislocation generation during warm laser shock peening process.

Declaration of Competing Interest

The authors declare that they have no known competing financial interests or personal relationships that could have appeared to influence the work reported in this paper.

Acknowledgement

Supplementary materials

Supplementary material associated with this article can be found, in the online version, at doi:10.1016/j.actamat.2022.118436.

References

[1] H. Kim, D.W. Suh, N.J. Kim, Fe-Al-Mn-C lightweight structural alloys: a review on the microstructures and mechanical properties, Sci. Technol. Adv. Mater. 14 (1) (2013).

[2] O.A. Zambrano, A general perspective of Fe-Mn-Al-C steels, Rev. A general perspective of Fe – Mn – Al – C steels (2018) June.

[3] C.L. Lin, C.G. Chao, J.Y. Juang, J.M. Yang, T.F. Liu, Deformation mechanisms in ultrahigh-strength and high-ductility nanostructured FeMnAlC alloy, J. Alloys Compd. 586 (2014) 616–620.

[4] K. Choi, et al., Effect of aging on the microstructure and deformation behavior of austenite base lightweight Fe-28Mn-9Al-0.8C steel, Scr. Mater. 63 (10) (2010) 1028–1031.

[5] S.E. Prameela, et al., Deformation assisted nucleation of continuous nanoprecipitates in Mg–Al alloys, Materialia 9 (December 2019) 2020.

[6] S.H. Kim, H. Kim, N.J. Kim, Brittle intermetallic compound makes ultrastrong low-density steel with large ductility, Nature 518 (7537) (2015) 77–79.

[7] S. Sridhar, S. Clark, V. Janik, A. Rahnama, H. Kotadia, Nano-mechanical properties of Fe-Mn-Al-C lightweight steels, Sci. Rep. 8 (1) (2018) 1–12.

[8] J. Frieden, A. Przeworski, General introduction, Sel. Work. Michael Wallerstein Polit. Econ. Inequality, Unions, Soc. Democr. (2008) 1–6.

[9] S. Xiang, et al., Understanding the role of monolayer graphene during long range shock strengthening of metal-graphene heterostructure, Mater. Sci. Eng. A 837 (2021) 142741 September2022.

[10] Y. Liao, C. Ye, B.J. Kim, S. Suslov, E.A. Stach, G.J. Cheng, Nucleation of highly dense nanoscale precipitates based on warm laser shock peening, J. Appl. Phys. 108 (6) (2010) 1–8.

[11] C. Ye, Y. Liao, S. Suslov, D. Lin, G.J. Cheng, Ultrahigh dense and gradient nano–precipitates generated by warm laser shock peening for combination of high strength and ductility, Mater. Sci. Eng. A 609 (2014) 195–203.

[12] C. Ye, S. Suslov, B.J. Kim, E.A. Stach, G.J. Cheng, Fatigue performance improvement in AISI 4140 steel by dynamic strain aging and dynamic precipitation during warm laser shock peening, Acta Mater 59 (3) (2011) 1014–1025.

[13] N. Zhou, C. Shen, M. Mills, Y. Wang, Large-scale three-dimensional phase field simulation of γ'-rafting and creep deformation, Philos. Mag. 90 (1–4) (2010) 405–436.

[14] X. Wu, Y. Li, M. Huang, W. Liu, Z. Hou, Precipitation kinetics of ordered γ' phase and microstructure evolution in a Ni[*sbnd*]Al alloy, Mater. Chem. Phys. 182 (2016) 125–132.

[15] G. Han, Z. Han, A.A. Luo, B. Liu, Three-dimensional phase-field simulation and experimental validation of β-Mg17Al12 phase precipitation in Mg-Al-based alloys, Metall. Mater. Trans. A Phys. Metall. Mater. Sci. 46 (2) (2015) 948–962.

[16] F. Wang, B. Nestler, A phase-field study on the formation of the intermetallic Al2Au phase in the Al-Au system, Acta Mater 95 (2015) 65–73.

[17] H.M. Zbib, T. Diaz de la Rubia, A multiscale model of plasticity, Int. J. Plast. 18 (9) (2002) 1133–1163.

[18] R.B. Sills, W.P. Kuykendall, A. Aghaei, and W. Cai, Fundamentals of dislocation dynamics simulations, vol. 245. 2016.

[19] G.J. Cheng, M.A. Shehadeh, Dislocation behavior in silicon crystal induced by laser shock peening: a multiscale simulation approach, Scr. Mater. 53 (9) (2005) 1013–1018.

[20] M.A. Shehadeh, H.M. Zbib, T.D. De La Rubia, Multiscale dislocation dynamics simulations of shock compression in copper single crystal, Int. J. Plast. 21 (12) (2005) 2369–2390.

[21] S. Queyreau, B. Devincre, Bauschinger effect in precipitation-strengthened materials: a dislocation dynamics investigation, Philos. Mag. Lett. 89 (7) (2009) 419–430.

[22] R. Wu and S. Sandfeld, "Some steps towards modelling of dislocation assisted rafting: coupled 2D phase held-continuum dislocation dynamics approach," 2016.

[23] S.G. Kim, W.T. Kim, T. Suzuki, Phase-field model for binary alloys, Phys. Rev. E - Stat. Physics, Plasmas, Fluids, Relat. Interdiscip. Top. 60 (6) (1999) 7186–7197.

[24] J. Miettinen, S. Koskenniska, V.V. Visuri, M. Somani, T. Fabritius, J. Kömi, Thermodynamic, kinetic, and microstructure data for modeling solidification of Fe-Al-Mn-Si-C alloys, Metall. Mater. Trans. B Process Metall. Mater. Process. Sci. 51 (6) (2020) 2946–2962.

[25] Y. Tsukada, A. Shiraki, Y. Murata, S. Takaya, T. Koyama, M. Morinaga, Phase–field simulation of nucleation and growth of M23C 6 carbide and ferromagnetic phases during creep deformation in Type 304 steel, J. Nucl. Mater. 401 (1–3) (2010) 154–158.

[26] K. Chu, M.E. Foster, R.B. Sills, X. Zhou, T. Zhu, D.L. McDowell, Temperature and composition dependent screw dislocation mobility in austenitic stainless steels from large-scale molecular dynamics, npj Comput. Mater. 6 (1) (2020).

[27] W. Pabst, E. Gregorova, Characterization of particles and particle systems, ICT Prague (2007) 1–122.

[28] A. Rahnama, H. Kotadia, S. Clark, V. Janik, S. Sridhar, Nano-mechanical properties of Fe-Mn-Al-C lightweight steels, Sci. Rep. 8 (1) (2018) 1–12.

[29] C.S. Smith, L. Guttman, Measurement of internal boundaries in three-dimensional structures by random sectioning, JOM 5 (1) (1953) 81–87.

[30] X.D. Ren, et al., Dislocation evolution and properties enhancement of GH2036 by laser shock processing: dislocation dynamics simulation and experiment, Mater. Sci. Eng. A 654 (2016) 184–192 December.

[31] Y. Song, D. Garcia-Gonzalez, A. Rusinek, Constitutive models for dynamic strain aging in metals: strain rate and temperature dependences on the flow stress, Materials (Basel) 13 (7) (2020).